

THE COUNTERJET OF HH 30: NEW LIGHT ON ITS BINARY DRIVING SOURCE

ROBERT ESTALELLA¹, ROSARIO LÓPEZ¹, GUILLEM ANGLADA², GABRIEL GÓMEZ^{3,4},
ANGELS RIERA^{5,1}, AND CARLOS CARRASCO-GONZÁLEZ^{2,6}

(Received; Accepted)
Printed November 5, 2018

ABSTRACT

We present new [SII] images of the HH 30 jet and counterjet observed in 2006, 2007, and 2010 that, combined with previous data, allowed us to measure with improved accuracy the positions and proper motions of the jet and counterjet knots. Our results show that the motion of the knots is essentially ballistic, with the exception of the farthest knots, which trace the large scale “C”-shape bending of the jet. The observed bending of the jet can be produced by a relative motion of the HH 30 star with respect to its surrounding environment, caused either by a possible proper motion of the HH 30 star, or by the entrainment of environment gas by the red lobe of the nearby L1551-IRS 5 outflow. Alternatively, the bending can be produced by the stellar wind from a nearby CTTS, identified in the 2MASS catalog as J04314418+181047. The proper motion velocities of the knots of the counterjet show more variations than those of the jet. In particular, we identify two knots of the counterjet that have the same kinematic age but whose velocities differ by almost a factor of two. Thus, it appears from our observations that counterjet knots launched simultaneously can be ejected with very different velocities. We confirm that the observed wiggling of the jet and counterjet arises from the orbital motion of the jet source in a binary system. Precession, if present at all, is of secondary importance in shaping the jet. We derive an orbital period $\tau_o = 114 \pm 2$ yr and a mass function $m\mu_c^3 = 0.014 \pm 0.006 M_\odot$. For a mass of the system of $m = 0.45 \pm 0.04 M_\odot$ (the value inferred from observations of the CO kinematics of the disk) we obtain a mass $m_j = 0.31 \pm 0.04 M_\odot$ for the jet source, a mass $m_c = 0.14 \pm 0.03 M_\odot$ for the companion, and a binary separation of $a = 18.0 \pm 0.6$ AU. This binary separation coincides with the value required to account for the size of the inner hole observed in the disk, which has been attributed to tidal truncation in a binary system.

Subject headings: ISM: Herbig-Haro objects — ISM: individual (HH 30) — ISM: jets and outflows — stars: formation —

1. INTRODUCTION

The Herbig-Haro (HH) object 30 (Mundt & Fried 1983), located in the northeastern part of the L1551 dark cloud, lies at a distance of 140 pc (Kenyon et al. 1994). The HH 30 outflow is considered a prototypical jet/disk system. It presents a clear jet/counterjet structure, which has been described by Mundt et al. (1987, 1988) and Graham & Heyer (1990). The HH 30 exciting source is an optically invisible star (Vrba et al. 1999) highly extinguished by an edge-on disk (Burrows et al. 1996; Stapelfeldt et al. 1999), which extends up to a radius of ~ 250 AU perpendicularly to the jet, and divides the surrounding reflection nebulosity into two lobes. Kenyon et al. (1998) propose a spectral type M0 for the HH 30 star, and Cotera et al. (2001) estimate a bolomet-

ric luminosity of 0.2–0.9 L_\odot . López et al. (1995, 1996) propose that a number of knots located to the northeast of the HH 30 object are also part of the same flow, resulting in a total angular size of $\sim 500''$ (~ 0.35 pc) for the whole outflow. Several studies have explored the spatial morphology along and across the jet axis (Mundt et al. 1991; Ray et al. 1996), the 3-D structure (Esquivel et al. 2007; De Colle et al. 2010), line ratios (Mundt et al. 1990; Bacciotti et al. 1999; Hartigan & Morse 2007), or radial velocities (Raga et al. 1997) of the HH 30 flow.

In addition, some studies have been carried out studying the variability of the reflection nebulosity around HH 30. Watson & Stapelfeldt (2007) find variations of the lateral asymmetry of the nebula and counternebula, but find no convincing evidence for any period. However, Durán-Rojas et al. (2009) find a periodic modulation of the polarization of the nebula, with a period of 7.5 days, which is interpreted as produced by asymmetric accretion hot spots on the star, or orbiting clumps or voids in the disk.

Proper motions of a few knots of the HH 30 flow were determined by Mundt et al. (1990), Burrows et al. (1996), and López et al. (1996). A thorough study of the proper motions of all the knots of the HH 30 jet and the closest knots of the counterjet was made by Anglada et al. (2007). The main result of this study is that the overall structure of the HH 30 jet can be well fitted by the shape of a wiggling ballistic jet, arising either by the orbital motion of the jet source or by precession

¹ Departament d’Astronomia i Meteorologia, Institut de Ciències del Cosmos (ICC), Universitat de Barcelona (IEEC-UB), Martí i Franquès 1, E-08028 Barcelona, Spain; robert.estalella@am.ub.es, rosario.lopez@am.ub.es

² Instituto de Astrofísica de Andalucía, CSIC, Glorieta de la Astronomía s/n, E-18008 Granada, Spain; guillem@iaa.es

³ Instituto de Astrofísica de Canarias, E-38200 La Laguna, Tenerife, Spain; ggv@iac.es

⁴ GTC; GRANTECAN S.A. (CALP), E-38712 Breña Baja, La Palma, Spain; gabriel.gomez@gtc.iac.es

⁵ Departament de Física i Enginyeria Nuclear, Escola Universitària d’Enginyeria Tècnica Industrial de Barcelona, Universitat Politècnica de Catalunya, Comte d’Urgell 187, E-08036 Barcelona, Spain; angels.riera@upc.edu

⁶ Max-Planck-Institut für Radioastronomie, Auf dem Hügel 69, 53121 Bonn, Germany

of the jet axis because of the tidal effects of a companion. In the first case the binary separation is expected to be 9–18 AU, while in the case of precession the binary separation is < 1 AU. Given that the radius of the flared disk observed in the HST images is 250 AU, the conclusion is that this disk appears to be a circumbinary disk rather than a circumstellar disk, contrary to what was initially thought. This circumbinary disk is unlikely to have a relevant role in the jet collimation.

Pety et al. (2006) carry out PdBI observations of the dust continuum and CO line emission revealing the presence of an asymmetric molecular outflow and a disk in Keplerian rotation, deriving a central stellar mass of $0.45 \pm 0.04 M_{\odot}$. More recently, Guilloteau et al. (2008) carry out CO and dust continuum observations of the circumbinary disk that reveal an inner cavity with a radius of 37 ± 4 AU, and Madlener et al. (2012), through a detailed modeling, conclude that the disk has an inner depletion zone with a similar radius of 45 ± 5 AU radius. Guilloteau et al. (2008) explain the size of the inner hole as a result of tidal forces induced by a binary with a separation of 18 ± 2 AU, supporting the binary interpretation proposed by Anglada et al. (2007).

In this paper we present new [SII] images of the HH 30 jet and counterjet carried out in 2006, 2007, and 2010, which allowed us to measure the position and proper motion of the jet and counterjet knots, and to constrain the parameters of the binary system. In §2 we describe the observations; in §3 we describe the procedure used for the proper motions determination; in §4 we study the large-scale jet bending, and its possible origin; in §5 we analyze the jet wiggling and the constraints on the physical parameters of the binary system at the core of HH 30; finally, in §6 we discuss the results obtained and in §7 we give our conclusions.

2. OBSERVATIONS

The CCD observations used in this paper to determine the proper motions of the HH 30 jet/counterjet system are listed in Table 1. All the images were obtained through [SII] narrow-band filters, which included the $\lambda\lambda 6716, 6731$ Å emission lines. The details on the setup configuration, acquisition and treatment of the 2.5 m Isaac Newton Telescope (INT) image are given in López et al. (1995). All the images obtained at the 2.6 m Nordic Optical Telescope (NOT) were obtained using the same setup configuration (i.e. the Andalucía Faint Object Spectrograph and Camera, ALFOSC, and the [SII] filter centered on $\lambda = 6724$ Å and bandpass $\Delta\lambda = 50$ Å). More details on the acquisition and treatment of the NOT observations can be found in Anglada et al. (2007). Finally, the 2010 image was obtained at the 4.2 m William Herschel Telescope (WHT), using the ACAM camera on the Cassegrain focus, giving a field of view of $8'$ with a spatial scale of $\sim 0''.25$ pixel $^{-1}$. A narrow-band [SII] filter, centered on $\lambda = 6727$ Å and bandpass $\Delta\lambda = 48$ Å was used. In addition, a frame of a shorter exposure time of 3600 s was acquired through another narrow-band filter, centered on $\lambda = 6645$ Å and bandpass $\Delta\lambda = 50$ Å. This filter includes the nearby continuum, free of [SII] emission lines, useful to subtract the contribution of the continuum reflected emission close to the HH 30 jet source from the line emission image. For each epoch, several frames,

Table 1
[SII] images of the HH 30 jet/counterjet system

Epoch	Telescope/Instrument	Exp. time (s)	Reference
1993 Dec 15	INT	14400	1
1998 Nov 08	NOT/ALFOSC	9000	2
1999 Nov 20	NOT/ALFOSC	14400	2
2006 Jan 19	NOT/ALFOSC	14400	3
2007 Nov 06	NOT/ALFOSC	10800	3
2010 Dec 01	WHT/ACAM	12000	3

References. — (1) López et al. (1995) (2) Anglada et al. (2007) (3) This work

with a typical time exposure of 1800 s, were obtained to complete the total integration times, listed in Table 1, of the final deep images. The individual frames were processed using the standard tasks of IRAF⁷ reduction package, which included bias subtraction and flat-field corrections, using sky flats. In order to correct for misalignments, all the individual frames of the same epoch were recentered using the position of field stars. Then, the frames were median-averaged to obtain a final deep image for each of the epochs listed in Table 1. Images were not flux calibrated.

The six final images were converted into a common reference system and rebinned to the same pixel scale. The positions of seven field stars, common to all the frames, were used to register the images. The GEOMAP and GEOTRAN tasks of IRAF were applied to perform a linear transformation, with six free parameters that take into account translation, rotation and magnification between different frames. All the transformed frames have a pixel size equal to that of the last epoch WHT image that was taken as the reference image.

Astrometric calibration of the images transformed to the common reference system was made by using the coordinates of ten field stars, well distributed on the observed field. The coordinates were obtained after identifying the stars from the 2MASS All Sky Catalogue. The high optical extinction of the region made it impossible to find such a grid of reference stars from the USNO-B1.0 Catalogue. The typical rms of the transformation was $\leq 0''.1$ in both coordinates. The pixel size was found to be $0''.2528$ pixel $^{-1}$.

3. PROPER MOTIONS

The images used for proper motion determination were rotated by an angle of $31^{\circ}6$, the position angle of the jet axis (Anglada et al. 2007), so that the y axis is along the jet axis and the x -axis is perpendicular, with values increasing from left to right. In order to improve the signal-to-noise ratio, the images were smoothed with a Gaussian with a FWHM of 3 pixels. The smoothed images were used for the farther away knots of the jet and counterjet (B to E, and J to N), while the full resolution images were used for the stronger, closer to the origin knots (A and Z). This nomenclature for the knots is based on that of López et al. (1995) and Anglada et al. (2007). Knots Z3 to Z6 of the counterjet, detected in our 2006, 2007,

⁷ IRAF is distributed by the National Optical Astronomy Observatories, which are operated by the Association of Universities for Research in Astronomy, Inc., under cooperative agreement with the National Science Foundation.

Table 2
Positions and Proper Motions of Knots in the HH 30 Jet

Knot	x^a (")	y^a (")	μ_x (" yr ⁻¹)	μ_y (" yr ⁻¹)	ϵ_x^b (")	ϵ_y^b (")	v_t^c (km s ⁻¹)	P.A. ^d (deg)
A1	-0.04	2.69	-0.005 ± 0.007	0.153 ± 0.010	0.06	0.08	101.5 ± 6.4	1.9 ± 2.6
A2	0.08	4.12	0.007 ± 0.007	0.150 ± 0.008	0.08	0.08	99.5 ± 5.1	-2.6 ± 2.8
A3	0.09	6.85	0.003 ± 0.003	0.179 ± 0.008	0.03	0.08	118.7 ± 5.1	-1.0 ± 0.9
B1	0.12	11.04	-0.005 ± 0.003	0.097 ± 0.006	0.03	0.06	64.5 ± 3.9	3.0 ± 1.9
B2	-0.10	13.49	-0.005 ± 0.002	0.193 ± 0.007	0.03	0.10	127.9 ± 4.5	1.5 ± 0.7
B3	-0.25	14.36	0.008 ± 0.008	0.190 ± 0.010	0.08	0.10	126.4 ± 6.8	-2.4 ± 2.5
C	-0.30	17.12	-0.005 ± 0.003	0.177 ± 0.017	0.04	0.24	117.3 ± 11.4	1.6 ± 1.0
D1	0.05	21.19	0.009 ± 0.007	0.319 ± 0.028	0.07	0.29	212.1 ± 18.6	-1.5 ± 1.3
D2	0.06	24.31	-0.005 ± 0.007	0.382 ± 0.024	0.10	0.33	253.8 ± 15.8	0.7 ± 1.1
D3	0.09	27.17	-0.008 ± 0.005	0.265 ± 0.098	0.02	0.34	175.9 ± 64.8	1.8 ± 1.2
D4	-0.33	29.64
E1	-0.60	35.81	-0.005 ± 0.002	0.149 ± 0.007	0.03	0.10	98.8 ± 4.7	2.0 ± 0.8
E2	0.60	41.05	-0.001 ± 0.009	0.099 ± 0.012	0.12	0.17	65.9 ± 7.9	0.8 ± 5.0
E3b	-0.55	48.03	-0.007 ± 0.009	0.199 ± 0.004	0.08	0.04	131.9 ± 2.9	1.9 ± 2.5
E4	-0.46	52.04	-0.020 ± 0.007	0.143 ± 0.003	0.10	0.05	95.8 ± 2.3	7.8 ± 2.7

^a Positions in the 2010 image, except for knot B3, for which the position is that of the 2007 image. The y axis is along the jet, at a position angle (eastwards from north) of 31°6. The (0,0) position is that of the brightest knot, A0.

^b Rms residual of the knot positions in the proper motion fit, $\epsilon = \sigma\sqrt{1-r^2}$, where σ is the standard deviation and r the correlation coefficient.

^c Proper motion velocity, assuming a distance of 140 pc.

^d Position angle with respect to the y direction.

Table 3
Positions and Proper Motions of Knots in the HH 30 Counterjet

Knot	x^a (")	y^a (")	μ_x (" yr ⁻¹)	μ_y (" yr ⁻¹)	ϵ_x^b (")	ϵ_y^b (")	v_t^c (km s ⁻¹)	P.A. ^d (deg)
Z1	0.05	-5.61	0.000 ± 0.010	-0.278 ± 0.012	0.08	0.13	184.8 ± 8.3	-179.9 ± 2.1
Z2	-0.05	-9.55	0.011 ± 0.001	-0.462 ± 0.003	0.01	0.03	307.0 ± 2.2	-178.7 ± 0.1
Z3	0.16	-11.71	0.065 ± 0.020	-0.223 ± 0.026	0.07	0.09	154.4 ± 17.1	-163.7 ± 5.1
Z4	-0.23	-13.43	-0.022 ± 0.022	-0.166 ± 0.055	0.08	0.19	111.0 ± 36.0	172.5 ± 8.0
Z5a	0.06	-17.41	0.046 ± 0.046	-0.227 ± 0.003	0.16	0.01	153.8 ± 6.4	-168.6 ± 11.3
Z5b	-0.10	-18.26	-0.027 ± 0.006	-0.316 ± 0.003	0.02	0.01	210.7 ± 1.9	175.1 ± 1.0
Z6	0.16	-23.65	0.012 ± 0.016	-0.608 ± 0.084	0.05	0.29	403.3 ± 55.5	-178.9 ± 1.5
J	0.32	-78.30	0.029 ± 0.013	0.066 ± 0.060	0.17	0.78	48.0 ± 36.9	-23.6 ± 21.5
K1	1.56	-94.35	0.064 ± 0.016	-0.174 ± 0.057	0.20	0.73	122.9 ± 35.5	-159.8 ± 7.6
K2	0.89	-99.02	0.036 ± 0.012	-0.148 ± 0.032	0.16	0.42	101.3 ± 21.0	-166.4 ± 5.4
L	4.09	-149.00	0.004 ± 0.012	-0.249 ± 0.025	0.16	0.32	165.0 ± 16.6	-179.2 ± 2.8
M	7.23	-176.61	0.011 ± 0.008	-0.325 ± 0.015	0.10	0.20	215.9 ± 10.2	-178.0 ± 1.4
N	11.59	-191.00	0.076 ± 0.003	-0.323 ± 0.015	0.04	0.19	220.1 ± 9.5	-166.7 ± 0.8

^a Positions in the 2010 image. The y axis is along the jet, at a position angle of 31°6. The (0,0) position is that of the brightest knot, A0.

^b Rms residual of the knot positions in the proper motion fit, $\epsilon = \sigma\sqrt{1-r^2}$, where σ is the standard deviation and r the correlation coefficient.

^c Proper motion velocity, assuming a distance of 140 pc.

^d Position angle with respect to the y direction.

and 2010 observations, have been identified for the first time. Positions of the knots for each epoch were measured with respect to the position of the brightest knot A0, whose position was set to $(x, y) = (0, 0)$. The position of the knots was determined from a parabolic fit to the intensity of the 5×5 pixels centered on the pixel with peak emission. Then, the proper motion in x and y directions of each knot, μ_x and μ_y , was determined from a linear regression fit to their positions in the different epoch images.

The 1993 image has poorer seeing than the others, and could not be used for knots close to the HH 30 star, i.e. knots A and Z. The 1989 and 1999 images do not include the counterjet region for distances greater than 5''6, and could not be used neither for the counterjet knots Z3 to

Z6, nor for J to N. The results are given in Tables 2 and 3, and shown in Fig. 1, where the knot positions and proper motions are shown superimposed on the smoothed 2010 image.

The errors assigned to the proper motions, in both x and y , are the formal errors of the slope of the linear regression fits for each knot. These errors are shown as ellipses at the end of the arrows shown in Fig. 1. The errors appear to be rather small as a consequence of the wide span of time used for calculating the proper motions, and that 6 epochs were used for most knots. The quality of the linear regression fits for each knot is indicated by the small values of the residuals in x , ϵ_x , and y , ϵ_y , (see Tables 2 and 3) and is illustrated in Fig. 2, where the measured and fitted values of the y position

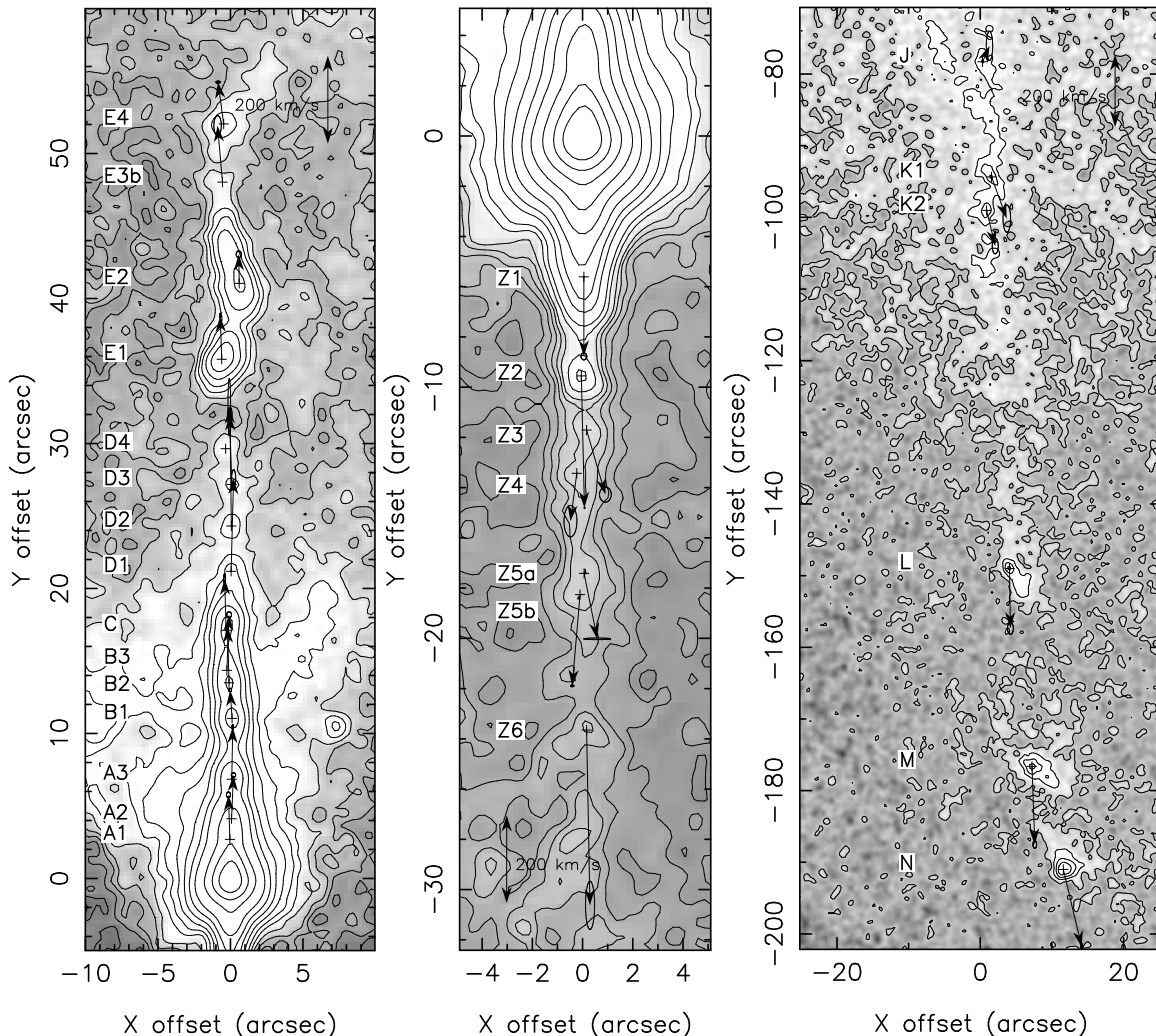


Figure 1. 2010 [SII] narrow-band image of the jet and counterjet of HH 30, smoothed with a 3-pixel Gaussian, showing the proper motion velocities of the knots A to E (*left*); knots Z (*center*); and knots J to N (*right*). The y axis is along the jet axis, at a position angle of $31^\circ 6'$.

as a function of time for each knot, are shown. In all the cases, the y positions are well fitted by the proper motion velocity obtained, showing that the motion of the knots is ballistic.

All the knots show proper motions roughly in the direction of the jet axis, with the exception of knot J of the counterjet, which has been measured to be nearly stationary. This knot is located inside a reflection nebulosity southwest of the HH 30 star (spreading from $y \simeq -25''$ to $-100''$; see Fig. 1), and is most probably not a counterjet knot, but a feature of the reflection nebulosity. We will not consider this knot in the following.

It is worth noting that the proper motions μ_y obtained here are significantly lower than those obtained in Anglada et al. (2007) from two observations with nearly one year of interval, in 1998 and 1999. On the average, the proper motion velocities for knots A to E of the jet are $0''.11 \text{ yr}^{-1}$ (or 75 km s^{-1}) higher in Anglada et al. (2007) than the present values. For the counterjet, the absolute value of the proper motion velocities for knots Z1 and Z2 are $0''.13 \text{ yr}^{-1}$ (or 85 km s^{-1}) lower in Anglada et al. (2007) than the present values. Since the proper motions are measured with respect to the brightest knot A0, the discrepancy can be explained by a shift in the

position of A0 along the axis of the jet of $\Delta y \simeq -0''.12$ in the 1999 image with respect to that of 1998. Such a shift in position can be attributed to the observed variations in the brightness of the diffuse light of the HH 30 star (Watson & Stapelfeldt 2007; Durán-Rojas et al. 2009). However, this systematic error in the determination of proper motions is not expected to affect measurements that span over a large number of years, like those presented in the present work.

In Fig. 3 we plot the proper motion velocity in the y direction, in absolute value, $|v_y|$, as a function of distance y . As can be seen, the jet and counterjet velocities are quite different. For the jet knots, most have velocities $\sim 100 \text{ km s}^{-1}$, except knots D, with distances from the HH 30 star between $20''$ and $30''$, which have a higher velocity, $\sim 240 \text{ km s}^{-1}$. For the counterjet, the velocities are more irregular. There are knots with $|v_y| \simeq 100 \text{ km s}^{-1}$ (Z4), with $|v_y| \simeq 180 \text{ km s}^{-1}$ (Z1, Z3, Z5a, Z5b), and with $|v_y| > 300 \text{ km s}^{-1}$ (Z2, Z6). On the average, the proper motion velocity of the jet knots is 115 km s^{-1} , while for the counterjet knots the average is 193 km s^{-1} . The difference is also found in the velocity dispersion, which is 54 km s^{-1} for the jet, and 82 km s^{-1} for the counterjet. Thus, the counterjet knots have, on aver-

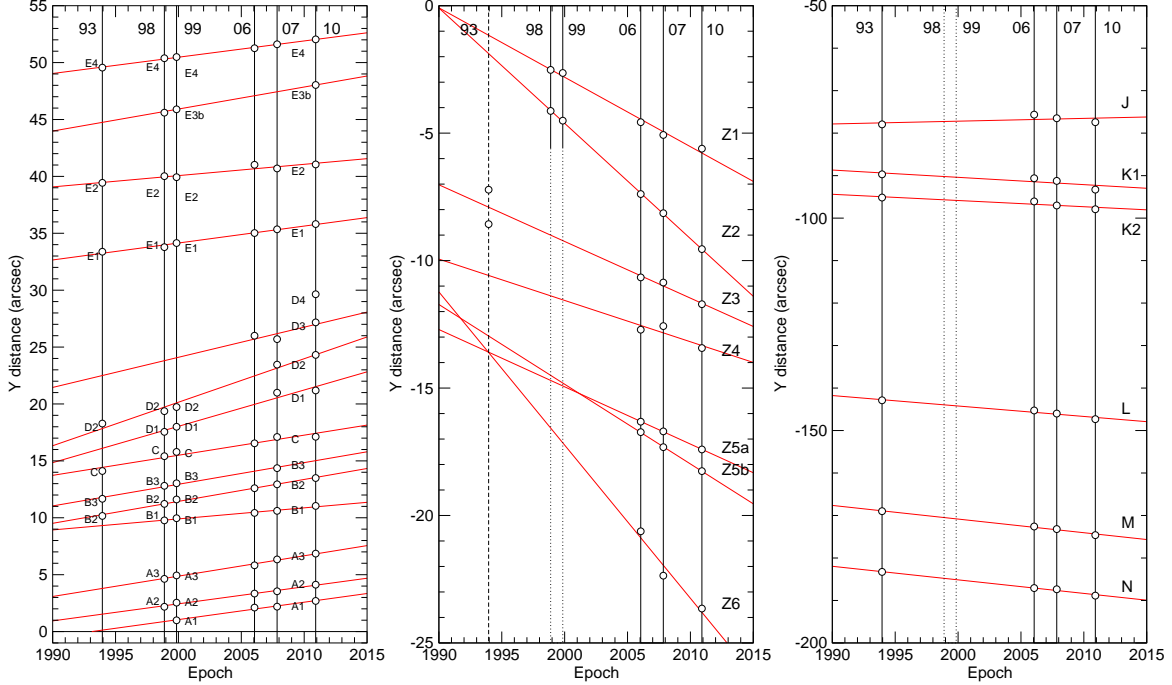


Figure 2. Diagram showing the y position of the knots of the jet and counterjet, as a function of time: knots A to E (*left*); knots Z (*center*); and knots J to N (*right*). The red lines show the linear fits used to derive the proper motion velocity in the y direction. The positions of 1993 have not been used for the proper motion determination of knots Z. The 1998 and 1999 images only reach up to $y = -5''.6$ from the HH 30 star in the counterjet.

age, higher velocities than the jet knots, and show more variation from knot to knot.

Let us now consider the pair of knots of the counterjet Z1 and Z2. The velocity of Z2 ($307 \pm 2 \text{ km s}^{-1}$) is much higher than that of Z1 ($185 \pm 8 \text{ km s}^{-1}$). This pair of knots, in spite of being very close to the HH 30 star, have well determined proper motions, since they have been observed at five epochs, spanning 17 years. In addition, the proper motions obtained by fitting only the new observations in 2006, 2007, and 2010, coincide with those obtained when the old observations of 1998 and 1999 are included in the fit. The positions of the two knots Z1 and Z2, when extrapolated back in time, show that they were launched simultaneously, at the end of 1989 (see Fig. 2). A similar case is found for the pair of knots Z5 and Z6 of the counterjet, but in this case the proper motion velocities are not so well constrained as in the case of Z1 and Z2. Thus, it appears that the counterjet of HH 30 is able to launch simultaneously pairs of knots with very different velocities.

In order to investigate the launching properties of all the knots, we calculated for each knot its kinematic age, $t_{\text{kin}} \simeq y/\mu_y$, and the position at launch, $x_{\text{lch}} \simeq x - \mu_x t_{\text{kin}}$. The results obtained are shown in Table 4. In Fig. 4 we show the x position at launch, x_{lch} , as a function of distance to the origin, $|y|$. As can be seen, all knots, except the more distant knots, have values of x_{lch} consistent with zero. This is an indication that these knots are ballistic, moving along a straight line after their launching. For the more distant knots, K1, K2, and N, $x_{\text{lch}} \simeq -30''$, indicating that they deviate from a straight line after their launching. As we will see in §4, the more distant knots trace the large-scale ‘‘C’’-shape bending of the jet and counterjet.

Table 4
Launch properties of knots in the HH 30 jet and counterjet

Knot	$t_{\text{kin}}^{\text{a}}$ (yr)	$x_{\text{lch}}^{\text{b}}$ (arcsec)
E4	364.1 ± 1.3	6.7 ± 2.5
E3b	248.3 ± 8.4	3.7 ± 3.3
E2	413.7 ± 4.9	1.1 ± 3.6
E1	240.8 ± 1.7	0.7 ± 0.5
D4
D3	102.6 ± 10.0	1.0 ± 0.6
D2	63.6 ± 1.5	0.4 ± 0.5
D1	66.3 ± 1.9	-0.5 ± 0.5
C	96.9 ± 1.7	0.2 ± 0.3
B3	75.4 ± 0.8	-0.8 ± 0.6
B2	70.0 ± 0.5	0.2 ± 0.2
B1	113.6 ± 0.7	0.7 ± 0.4
A3	38.3 ± 0.3	0.0 ± 0.1
A2	27.5 ± 0.2	-0.1 ± 0.2
A1	17.6 ± 0.2	0.1 ± 0.1
Z1	20.1 ± 0.3	0.0 ± 0.2
Z2	20.6 ± 0.1	-0.3 ± 0.1
Z3	52.4 ± 1.4	-3.3 ± 1.1
Z4	81.0 ± 4.4	1.6 ± 1.9
Z5a	76.6 ± 0.2	-3.4 ± 3.6
Z5b	57.7 ± 0.2	1.5 ± 0.3
Z6	38.9 ± 3.3	-0.3 ± 0.6
K1	543.0 ± 30.8	-33.1 ± 14.2
K2	667.6 ± 21.7	-23.0 ± 9.8
L	599.2 ± 15.0	1.9 ± 7.3
M	543.2 ± 8.3	1.0 ± 4.2
N	592.0 ± 8.7	-33.6 ± 2.7

^a Kinematic age defined as $t_{\text{kin}} = y/\mu_y$.

^b Offset position at launch, defined as $x_{\text{lch}} = x - \mu_x t_{\text{kin}}$.

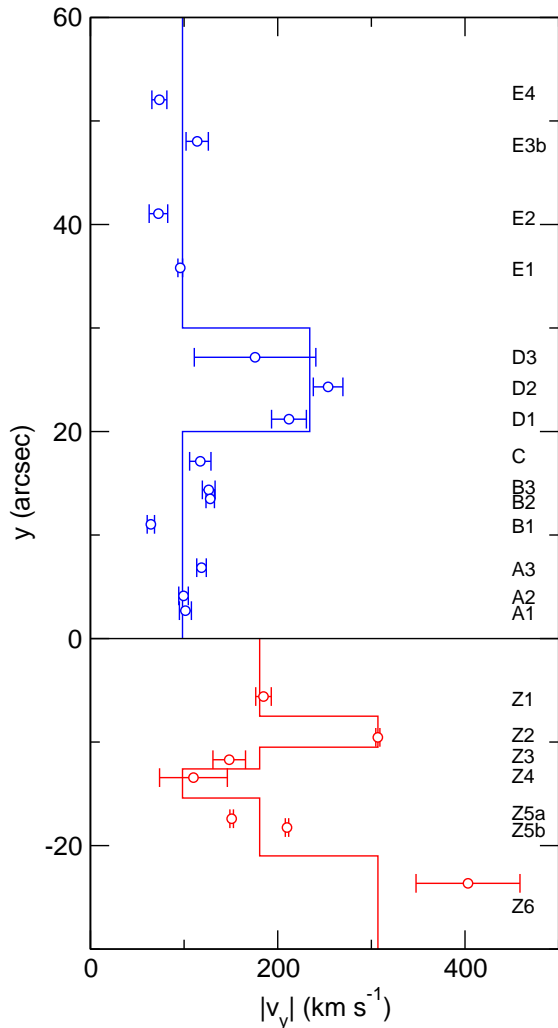


Figure 3. Proper motion velocity in the y direction (absolute value), $|v_y|$, versus distance, y , for the knots in the HH 30 jet (blue) and counterjet (red). The stepped lines indicate the velocities adopted for the knots of the jet (blue) and counterjet (red). These velocities are the error-weighted averages of the velocity of the knots in each step: $v_j = 98 \text{ km s}^{-1}$ (A, B, C, E, Z4); $v_j = 181 \text{ km s}^{-1}$ (Z1, Z3, Z5); $v_j = 234 \text{ km s}^{-1}$ (D); and $v_j = 307 \text{ km s}^{-1}$ (Z2, Z6).

4. JET BENDING

4.1. Bending by a plane-parallel side wind

The bending of the HH 30 jet/counterjet, with a clear “C” shape, was reported by López et al. (1995) and Anglada et al. (2007). Now, with the observations of the counterjet presented in this work, we know the shape of the jet/counterjet for a length of $\sim 500''$, corresponding to $\sim 0.35 \text{ pc}$.

The bending of the HH 30 jet is suggestive of being entrained toward the north-west (increasing x). This could be due to a proper motion of the HH 30 star toward the south-east with respect to the ambient medium. Cantó & Raga (1995) estimate that a relative velocity between the HH 30 star and the surrounding environment of $\sim 2 \text{ km s}^{-1}$ is sufficient for explaining the observed bending of the HH 30 jet/counterjet. Such a relative velocity could be the result of a proper motion of the HH 30 star of $\sim 0''.003 \text{ yr}^{-1}$, clearly below our accuracy in the proper motion measurements, of the order

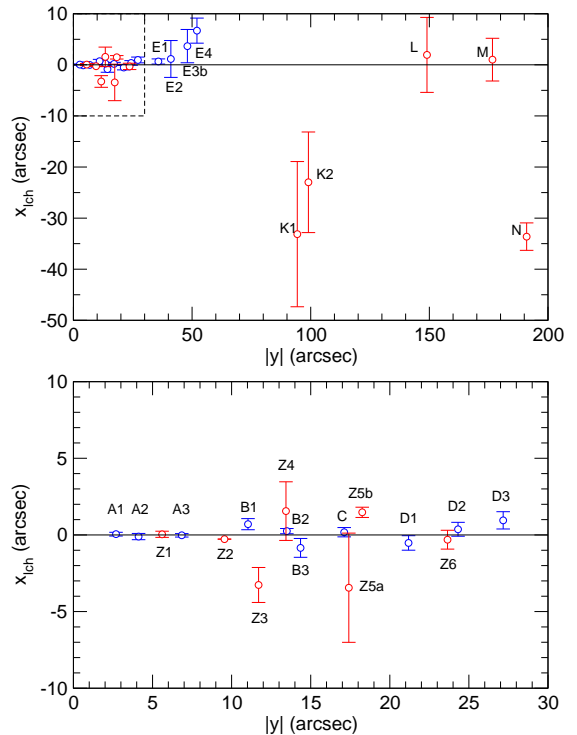


Figure 4. Position in the x axis at the epoch of launch assuming ballistic motions, $x_{\text{1ch}} = x - y \mu_x / \mu_y$, versus $|y|$ for the knots in the HH 30 jet (blue) and counterjet (red). *Top:* All knots. The dashed line shows the region that appears enlarged in the bottom panel. *Bottom:* Knots close to the origin.

of $\sim 0''.1 \text{ yr}^{-1}$. An alternative is that the deflection is caused by the powerful bipolar outflow whose exciting source, L1551-IRS5, is at a distance of $\sim 4'$ southwards of HH 30. The red lobe of the L1551-IRS5 molecular outflow is found to the south-east of the HH 30 star, and could be responsible of entraining the surrounding environment with a velocity of $\sim 2 \text{ km s}^{-1}$ and deflecting the jet and counterjet of HH 30.

A different explanation for the bending of the HH 30 jet and counterjet is a deflection by an isotropic stellar wind blowing the HH 30 jet from the south-east. In the following we will examine this possibility.

4.2. Bending by an isotropic stellar wind

We will use the model of jet deflection by an isotropic stellar wind, developed by Raga et al. (2009a), to fit the shape of the HH 30 jet/counterjet. The path of the jet/counterjet in a reference system centered on the wind source (see Fig. 5), is given in polar coordinates by

$$r(\phi) = \frac{r_s}{\cos^\lambda(\phi/\lambda)}, \quad -\lambda \frac{\pi}{2} < \phi < \lambda \frac{\pi}{2}, \quad (1)$$

where r_s is the distance from the wind source to the “stagnation point” (i.e. the point closest to the wind source) of the jet/counterjet system, and

$$\lambda \equiv \frac{\epsilon}{1 + \epsilon}, \quad 0 < \lambda < 1, \quad (2)$$

with ϵ given by

$$\epsilon = 2 \left(\frac{\dot{M}_j v_j}{\dot{M}_w v_w} \right)^{1/2} \frac{v_j}{c_j}, \quad (3)$$

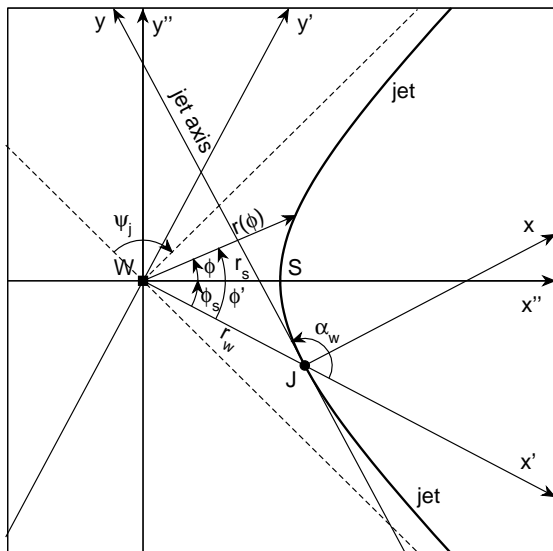


Figure 5. Reference systems used for studying the jet and counterjet bending. The jet path is indicated by the thick continuum line. The jet source, J , is indicated with a small circle, while the wind source, W , is indicated with a small square. The “stagnation point” is S . The distance from the side-wind source to S is r_s , and to J is r_w . The angle α_w is the angle between the x' and y axes, and ϕ_s is the angle with vertex at W , subtended by the jet source J and the stagnation point S . The reference system (x', y') is rotated an angle ϕ_s with respect to (x'', y'') . The reference system (x, y) is shifted a distance r_w and rotated an angle $\alpha_w - \pi/2$ with respect to (x', y') . The two dashed lines indicate the asymptotes to the jet and counterjet. The total deflection of the jet, ψ_j , is the angle between the two asymptotes.

where \dot{M}_j , v_j and c_j are the mass-loss rate, velocity and isothermal sound speed of the jet, and \dot{M}_w , v_w are the mass-loss rate and velocity of the wind. The parameter λ can be expressed in terms of the total deflection angle of the jet/counterjet path, ψ_j (see Fig. 5),

$$\lambda = 1 - \frac{\psi_j}{\pi}. \quad (4)$$

Let us call r_w the distance from the jet source to the wind source, and α_w the angle between the jet axis (y axis) and the direction from the wind source to the jet source (x' axis). As shown by Raga et al. (2009a), the angle ϕ_s , with vertex at the wind source and subtended by the jet source and the stagnation point (see Fig. 5), is given by.

$$\phi_s = \lambda(\alpha_w - \frac{\pi}{2}). \quad (5)$$

The polar equation of the jet shape in the reference system (x', y') is given by

$$r(\phi') = r_w \left[\frac{\sin \alpha_w}{\sin(\alpha_w - \phi'/\lambda)} \right]^\lambda, \quad \lambda(\alpha_w - \pi) < \phi' < \lambda\alpha_w. \quad (6)$$

Therefore, the coordinates of the jet shape in the reference system (x, y) , centered on the jet source and with the y axis along the tangent to jet/counterjet path, are given by

$$\begin{aligned} x &= [r(\phi') \cos \phi' - r_w] \sin \alpha_w - r(\phi') \sin \phi' \cos \alpha_w, \\ y &= [r(\phi') \cos \phi' - r_w] \cos \alpha_w + r(\phi') \sin \phi' \sin \alpha_w. \end{aligned} \quad (7)$$

The jet shape described by Eqs. 6 and 7 depends on three parameters: the distance to the wind source, r_w ;

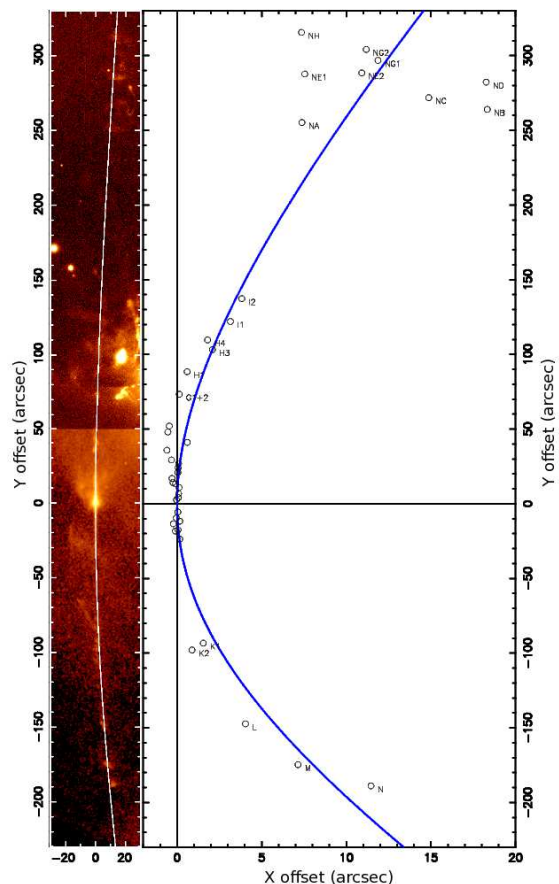


Figure 6. Bending of the HH 30 jet and counterjet. *Right:* The small circles mark the positions of the knots of the HH 30 jet and counterjet, with the farther knots labeled. The continuum line shows the best fit to the knot positions using the Raga et al. (2009a) model of jet bending by an isotropic stellar side wind. The x scale is amplified a factor of ~ 10 . *Left:* Best fit superposed on a [SII] image of the jet and counterjet. The upper half-image is from 1999 (Anglada et al. 2007) and the lower half-image is from 2010 (present work). The x and y scales are the same.

the angle between the jet axis and the direction to the wind source, α_w ; and the total deflection angle, ψ_j (or λ , related through Eq. 4).

A least-squares fit of the three free parameters of the model was performed to the positions of 43 knots, NA to NH from Anglada et al. (2007), knots A1 to I2 of the jet, and Z1 to N of the counterjet (present work), spanning a total length along the jet axis of $\sim 500''$.

The best fit was obtained for $r_w = 173'' \pm 15''$ (24200 ± 2100 AU in projection), $\alpha_w = 66^\circ \pm 4^\circ$, $\psi_j = 14^\circ 8' \pm 0^\circ 7'$ (corresponding to $\lambda = 0.918 \pm 0.004$), with an rms fit residual in x of $\epsilon_{\text{fit}} = 2''.22$ (see Fig. 6). The errors quoted were estimated as the increment in each parameter that increases the rms fit residual a factor of $(1 + \chi^2_3/n)^{1/2}$, where n is the number of points fitted, and χ^2_3 is the value of χ^2 for 3 degrees of freedom (the number of free parameters) and 68% significance ($1-\sigma$ uncertainty), $\chi^2_3 = 3.53$ (Lampton et al. 1976). For these values of the parameters we obtain that the stagnation point is located at $(x, y) = (+0''.8, -64'')$ (S position in Fig. 7). The wind source is located at a position $(x, y) = (-158'', -70'')$ (W position in Fig. 7). Within the $1-\sigma$ uncertainty ellipse of the W position we found a reddened star, identified in the 2MASS catalog (J04314418+181047), with coordinates

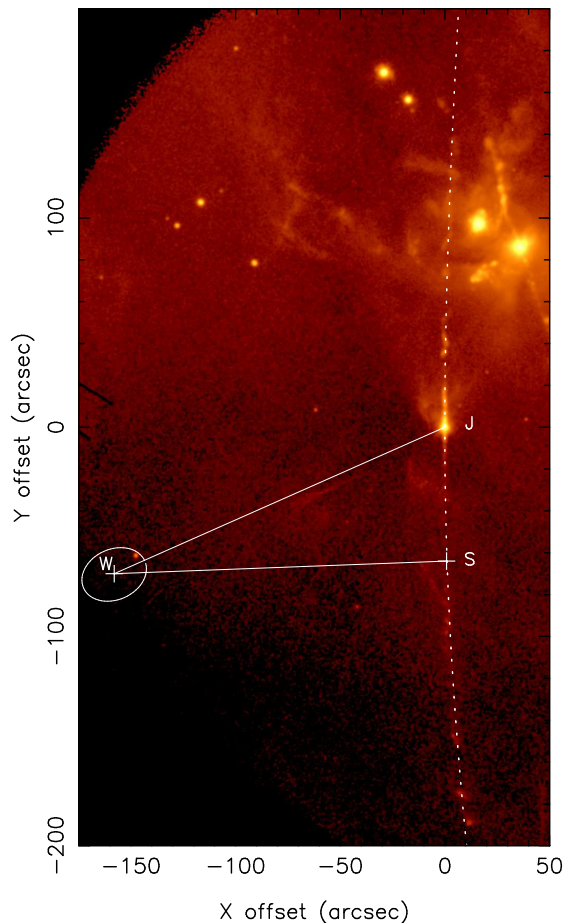


Figure 7. Bending of the HH 30 jet and counterjet by an isotropic stellar wind. The dotted line shows the best fit using the Raga et al. (2009a) model. The positions of the HH 30 star (J), wind source (W) and stagnation point (S) are indicated. The wind source is located at an offset position $(-158'', -70'')$. The ellipse shows the $1\text{-}\sigma$ uncertainty (68% confidence) in the position of W . The stagnation point is located at $(+0''.8, -64'')$.

$\alpha(J2000) = 04^{\text{h}}31^{\text{m}}44^{\text{s}}.180$, $\delta(J2000) = +18^{\circ}10'14''.78$, whose colors ($J - H = 1.33$, $H - K = 0.81$) correspond to those of a Classical T Tauri star (CTTS) in the $(J - H)$, $(H - K)$ diagrams (Lada & Adams 1992; Roman-Lopes 2009).

The total deflection of the jet, $\psi_j = 14^{\circ}8 \pm 0^{\circ}7$, implies a value of the parameter $\epsilon = 11.2 \pm 0.6$. As stated in Eq. 3, ϵ is related to the physical properties of the jet and the wind source. Taking a jet velocity $v_j = 100 \text{ km s}^{-1}$, and an isothermal sound speed of the jet $c_j = 10 \text{ km s}^{-1}$, we obtain

$$\frac{\dot{M}_j v_j}{\dot{M}_w v_w} = \left(\frac{\epsilon c_j}{2 v_j} \right)^2 = 0.31 \pm 0.02. \quad (8)$$

The mass-loss rate of the HH 30 jet and counterjet has been estimated to be $\dot{M}_j \simeq 2.6 \times 10^{-9} M_{\odot} \text{ yr}^{-1}$ (Bacciotti et al. 1999). For a jet velocity $v_j = 100 \text{ km s}^{-1}$, the HH 30 momentum rate is $\dot{M}_j v_j \simeq 2.6 \times 10^{-7} M_{\odot} \text{ yr}^{-1} \text{ km s}^{-1}$. Thus, the wind source needed to deflect the jet has to have a momentum rate

$$\dot{M}_w v_w \simeq (8.3 \pm 0.5) \times 10^{-7} M_{\odot} \text{ yr}^{-1} \text{ km s}^{-1}. \quad (9)$$

Mass-loss rates for CTTS in Taurus are of the order of $\dot{M}_w \simeq 10^{-10} - 10^{-8} M_{\odot} \text{ yr}^{-1}$, and up to one order of mag-

nitude higher for continuum CTTS (Hartmann 2005). Typical CTTS wind velocities are of the order of 100 km s^{-1} . Thus, for a CTTS we can expect

$$\dot{M}_w v_w \simeq 10^{-8} - 10^{-6} M_{\odot} \text{ yr}^{-1} \text{ km s}^{-1}. \quad (10)$$

This range of momentum rates encompasses the value needed to cause the observed deflection of the jet, given by Eq. 9. Thus, the star J04314418+181047 could be the wind source responsible for the deflection of the HH 30 jet, provided its mass-loss rate falls in the higher end of values found for CTTS.

If a CTTS can produce the observed bending of HH 30, this would imply that a vast majority of jets should be bent, since low-mass protostars are abundant. However, the bending of a jet is not easy to detect since it is only noticeable when the jet is imaged over a long length. In the case of HH 30, the images span a length of $500''$, or 0.35 pc .

5. JET WIGGLING

Following the work of Anglada et al. (2007), we consider that the wiggling of the HH 30 jet and counterjet is a consequence of the presence of a companion star to the jet source. Anglada et al. (2007), using the formulation given by Masciadri & Raga (2002), analyze the extreme cases where the dominant effect is either the orbital motion of the jet source in a binary system, or the precession of the ejection axis of the jet because of tidal interactions between the disk where the jet originates and a companion star. Here we develop the work of Raga et al. (2009b), and we consider a physical system, in which both the orbital motion and precession can be present simultaneously, to fit the HH 30 jet and counterjet wiggling shape.

5.1. Orbital and precession periods

We consider a binary system with a circular orbit, being m_j the mass of the jet source, m_c the mass of the companion, and $m = m_j + m_c$ the total mass of the system. We will call μ_c the mass of the companion relative to the total mass, so that

$$\begin{aligned} m_j &= (1 - \mu_c) m, \\ m_c &= \mu_c m. \end{aligned} \quad (11)$$

Let a be the binary separation (i.e. the radius of the relative orbit). Therefore, the orbital radius of the jet source with respect to the binary's center of mass (i.e. the radius of the jet source absolute orbit) is

$$r_o = \mu_c a, \quad (12)$$

and the orbital velocity of the jet source is given by

$$v_o = \frac{2\pi r_o}{\tau_o}, \quad (13)$$

where τ_o is the orbital period. The total mass of the binary system is related to τ_o , and μ_c , r_o , or a , through Kepler's third law,

$$\left(\frac{m}{M_{\odot}} \right) = \mu_c^{-3} \left(\frac{r_o}{\text{AU}} \right)^3 \left(\frac{\tau_o}{\text{yr}} \right)^{-2} = \left(\frac{a}{\text{AU}} \right)^3 \left(\frac{\tau_o}{\text{yr}} \right)^{-2}. \quad (14)$$

Let us consider that the disk of the jet source is tilted an angle β with respect to the orbital plane, and that it is

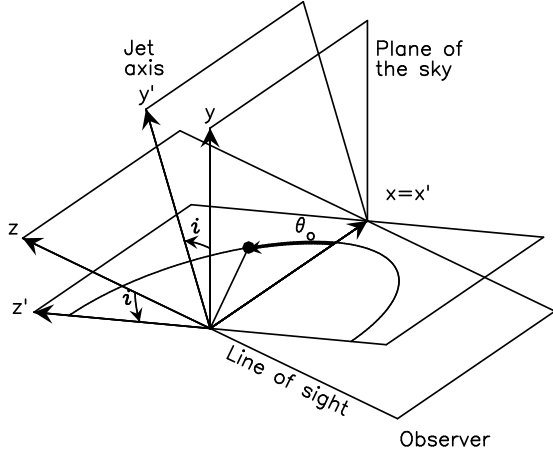


Figure 8. Reference systems used for studying the jet and counterjet wiggling. The jet axis has an inclination i with respect to the plane of the sky. The orbit is contained in the (x', y') plane. The orbital phase angle, θ_o , is measured counter-clockwise from the x' axis.

precessing with a period τ_p . An approximate expression relating the orbital and precession periods can be derived from Eq. 24 of Terquem (1998), valid for a disk precessing as a rigid body, by assuming that the disk surface density is uniform and that the rotation is Keplerian,

$$\frac{\tau_o}{\tau_p} = \frac{15}{32} \frac{\mu_c}{(1 - \mu_c)^{1/2}} \sigma^{3/2} \cos \beta, \quad (15)$$

where $\sigma = r_d/a$ is the ratio of disk radius to binary separation. Since it is expected that the size of the disk is truncated by tidal interaction with the companion star in such a way that $1/4 \leq \sigma \leq 1/2$ (Terquem 1998), we will adopt a value of $\sigma = 1/3$. With this value of σ , Eq. 15 gives: $\tau_o/\tau_p = 0.09(\mu_c/\sqrt{1 - \mu_c}) \cos \beta$. Note that, except for values of μ_c near to 1, the precession period is much longer than the orbital period.

5.2. Velocity and position of the knots as a function of time

For describing the jet we use a (linear) coordinate system (x', y', z') , with origin in the jet source, and where (x', z') is in the orbital plane, the x' -axis is the intersection of the orbital plane with the plane of the sky, and the y' -axis coincides with the orbital axis, at an inclination angle i with respect to the plane of the sky (pointing away from the observer). The coordinate system is illustrated in Fig. 8.

As in §3, for describing the observations we use an (angular) coordinate system (x, y, z) , where (x, y) is in the plane of the sky (the y -axis in the jet direction and the x -axis perpendicular with values increasing from left to right), and the z -axis points away from the observer (see Fig. 8). The transformations between both systems of coordinates are

$$x = \frac{x'}{D}, \quad y = \frac{y' \cos i - z' \sin i}{D}, \quad (16)$$

where D is the distance from the source to the observer, which accounts for the linear to angular transformation.

Let us assume that the velocity of the jet has a component perpendicular to the disk plane, v_j , and a component in the orbital plane, caused by the orbital motion

of the jet source, v_o . The components of the velocity of a jet parcel, or knot, are

$$\begin{aligned} v_{x'} &= -v_o \sin \theta_o \pm v_j \sin \beta \cos \theta_p, \\ v_{y'} &= \pm v_j \cos \beta, \\ v_{z'} &= v_o \cos \theta_o \pm v_j \sin \beta \sin \theta_p, \end{aligned} \quad (17)$$

with the sign of the v_j term being positive for $y' > 0$, and negative for $y' < 0$. The angles θ_o and θ_p are the orbital and precession phase angles, measured from the x' axis (perpendicular to the line of sight), at the epoch of launch, t_{lch} , when the jet parcel was ejected,

$$\begin{aligned} \theta_o &= \frac{2\pi}{\tau_o} (t_{\text{lch}} - t_0) + \varphi_o, \\ \theta_p &= -\frac{2\pi}{\tau_p} (t_{\text{lch}} - t_0) + \varphi_p, \end{aligned} \quad (18)$$

where φ_o, φ_p (between 0 and 2π) are the orbital and precession phase angles at an arbitrary epoch of reference, t_0 . Note that we assume that the precession is retrograde (see the discussion on retrograde precession in binary systems; Montgomery 2009), i.e. the orbital phase angle θ_o increases with time, while the precession phase angle θ_p decreases with time. The expression of Eq. 18 corresponds to orbital phase angles increasing from x' to z' (see Fig. 8), i.e. a counter-clockwise rotation as seen from positive values of y' (and clockwise for precession). In case of clockwise orbital rotation (and counter-clockwise precession), the orbital phase angle would decrease from x' to z' , and the velocity $v_{z'}$ (and the z' coordinate, see below), would have the opposite sign. The difference is only noticeable when the inclination angle i is large, since z' appears multiplied by $\sin i$ in the transformation given by Eq. 16.

The velocity of a jet parcel, or a knot, in the plane of the sky can be found from Eq. 17 by using a coordinate transformation similar to that of Eq. 16,

$$\begin{aligned} v_x &= -v_o \sin \theta_o \pm v_j \sin \beta \cos \theta_p, \\ v_y &= -v_o \cos \theta_o \sin i \pm v_j (\cos \beta \cos i - \sin \beta \sin \theta_p \sin i) \end{aligned} \quad (19)$$

The trajectory of this jet parcel, or knot, as a function of time is a straight line given by

$$\begin{aligned} x' &= r_o \cos \theta_o + (-v_o \sin \theta_o \pm v_j \sin \beta \cos \theta_p) (t - t_{\text{lch}}), \\ y' &= \pm v_j \cos \beta (t - t_{\text{lch}}), \\ z' &= r_o \sin \theta_o + (v_o \cos \theta_o \pm v_j \sin \beta \sin \theta_p) (t - t_{\text{lch}}). \end{aligned} \quad (20)$$

Note that the position of a knot at the epoch of its ejection ($t = t_{\text{lch}}$) is in the orbital plane ($y' = 0$). By using the coordinate transformation of Eq. 16 we obtain that the position of the knot in the plane of the sky, as a function of time, is given by

$$\begin{aligned} x &= \frac{1}{D} [r_o \cos \theta_o + (-v_o \sin \theta_o \pm v_j \sin \beta \cos \theta_p) (t - t_{\text{lch}})], \\ y &= \frac{1}{D} [-r_o \sin \theta_o \sin i + (-v_o \cos \theta_o \sin i \\ &\quad \pm v_j [\cos \beta \cos i - \sin \beta \sin \theta_p \sin i]) (t - t_{\text{lch}})]. \end{aligned} \quad (21)$$

5.3. Constant velocity jet: shape of the jet

If the jet velocity v_j is constant, all the knots have the same velocity, and the jet at a given epoch, $t = t_{\text{obs}}$, has

a shape that can be obtained by eliminating the time dependence of Eq. 20, substituting $t - t_{\text{ch}} = t_{\text{obs}} - t_{\text{ch}} = |y'|/(v_j \cos \beta)$ in the equations. The orbital and precession phase angles can be expressed as

$$\begin{aligned}\theta_o &= \frac{2\pi}{\tau_o} \left(t_{\text{obs}} - t_0 - \frac{|y'|}{v_j \cos \beta} \right) + \varphi_o, \\ \theta_p &= -\frac{2\pi}{\tau_p} \left(t_{\text{obs}} - t_0 - \frac{|y'|}{v_j \cos \beta} \right) + \varphi_p.\end{aligned}\quad (22)$$

For simplicity, we can introduce the parameter α (which plays a role similar to the angle of precession β),

$$\tan \alpha = \frac{v_o}{v_j \cos \beta}, \quad (23)$$

so that $v_o(t_{\text{obs}} - t_{\text{ch}}) = |y'| \tan \alpha$. The angle α is the half-opening angle of the jet in the (x', y') plane, containing the jet axis, in the absence of precession. With these changes, the shape of the jet is given by

$$\begin{aligned}x' &= r_o \cos \theta_o - |y'| \tan \alpha \sin \theta_o + y' \tan \beta \cos \theta_p, \\ z' &= r_o \sin \theta_o + |y'| \tan \alpha \cos \theta_o + y' \tan \beta \sin \theta_p.\end{aligned}\quad (24)$$

The shape of the jet in the plane of the sky (x, y) is obtained from the last equation, using the transformation of Eq. 16.

5.4. Variable velocity jet

The proper motions measured for the HH 30 knots (§3) show that the ejection velocity is significantly different for some knots. Let us consider that v_j (i.e. the ejection velocity component perpendicular to the disk plane), instead of being the same for the full jet, can be different for different parts of the jet. In this case, the jet has a shape composed of different parts moving at different velocities. Let us estimate the x position of each knot predicted by a model with given values of the parameters of the orbital motion (v_o, τ_o, φ_o), and of those of the precession (β, τ_p, φ_p).

For each knot we know, from our observations, its position, y , and proper motion, μ_y , along the jet axis. We can approximate the knot kinematic age by $t_{\text{kin}} \simeq y/\mu_y$. This approximation does not take into account the shift in position of the jet source caused by its orbital motion, so it holds for $y \gg r_o/D$, or for small inclination angles i . The epoch of launch of the knot is given by $t_{\text{ch}} = t_{\text{obs}} - t_{\text{kin}}$, and we can estimate the orbital and precession phase angles at the epoch of launch, given by Eq. 18. Once the orbital and precession phase angles are known, the ejection velocity component perpendicular to the disk plane for this knot, v_j , can be calculated from Eq. 19,

$$v_j = \frac{D\mu_y + v_o \cos \theta_o \sin i}{\cos \beta \cos i - \sin \beta \sin \theta_p \sin i}. \quad (25)$$

Therefore, the position of the knot in the plane of the sky at the epoch of observation ($t = t_{\text{obs}}$) can be obtained from Eq. 21, for $t - t_{\text{ch}} = t_{\text{kin}}$,

$$\begin{aligned}x &\simeq \frac{1}{D} [r_o \cos \theta_o + (-v_o \sin \theta_o + v_j \sin \beta \cos \theta_p) t_{\text{kin}}], \\ y &\simeq \frac{1}{D} [-r_o \sin \theta_o \sin i + (-v_o \cos \theta_o \sin i\end{aligned}\quad (26)$$

$$\begin{aligned}&+ v_j [\cos \beta \cos i - \sin \beta \sin \theta_p \sin i] t_{\text{kin}}] = \\ &= y - \frac{r_o}{D} \sin \theta_o \sin i.\end{aligned}$$

The first equation gives the x coordinate of the knot, and the second equation shows that the y coordinate of the knot is derived consistently by the model, for $y \gg r_o/D$, or for small inclination angles i .

5.5. Model parameters and limiting cases

In general, if the inclination angle i is known, and both orbital motion and precession can be fitted to the data, the model depends on six parameters, which can be chosen to be the mass function, $m\mu_c^3$ (see below), the orbital period, τ_o , the orbital phase angle at epoch t_0 , φ_o , the precession angle, β , the precession period, τ_p , and the precession phase angle at epoch t_0 , φ_p . The rest of parameters of the system can be obtained from these: μ_c is derived from Eq. 15; $m_j = (1 - \mu_c)m$, and $m_c = \mu_c m$ (Eq. 11); r_o and a are derived from Eq. 14; and v_o is derived from τ_o and r_o (Eq. 13).

The ‘‘pure’’ orbital model of § 4.1.1 of Anglada et al. (2007) corresponds to $\beta = 0$ in the previous equations (τ_p , and φ_p are undefined). In the case of a constant velocity jet, the shape of the jet (Eq. 24) has a plane symmetry (‘‘C’’ symmetry) with respect to the x axis. For such a ‘‘pure’’ orbital model, α (Eq. 23) is the half-opening angle of the jet cone, and the orbital period τ_o is determined by the jet velocity and the wavelength of the jet wiggles in the plane of the sky. However the total mass of the system, m , and the mass of the companion relative to the total mass, μ_c , cannot be determined independently, since the model depends only on the mass function $m\mu_c^3$ (Eq. 14). Thus, the ‘‘pure’’ orbital model depends on three parameters, which can be chosen to be the mass function, $m\mu_c^3$, the orbital period, τ_o , and the orbital phase angle at epoch t_0 , φ_o . This will be also the case of the general model when precession is not relevant in shaping the observed jet, for instance when the precession angle β is small compared to α , or when the wavelength of the wiggles caused by precession is longer than the length of the observed jet.

The ‘‘pure’’ precession model of § 4.1.2 of Anglada et al. (2007) is obtained from the previous equations in the limiting case $\mu_c \rightarrow 0$. For this limit the orbital radius r_o , the orbital velocity v_o , and α tend to zero, while the binary separation a and orbital period τ_o remain finite. In this case the orbital terms in Eqs. 24 and 26 vanish, and, in the case of a constant velocity jet, the shape of the jet has a point symmetry (‘‘S’’ symmetry) with respect to the origin. However, for a real system ($\mu_c > 0$), there is always orbital motion, even if precession is dominant. For such a precession-dominant model ($\alpha \ll \beta$), the precession angle β is the half-opening angle of the jet cone, and the precession period τ_p is determined by the jet velocity and the wavelength of the jet wiggles in the plane of the sky. Thus, three parameters, the precession angle, β , the precession period, τ_p , and the precession phase angle at epoch t_0 , φ_p , can be obtained from the fit. Then, for each value of μ_c in the interval $0 < \mu_c < 1$, an orbital period τ_o is obtained from Eq. 15 and, since $\alpha \ll \beta$, the following upper limits are found for the

binary separation, a , (Eqs. 12, 13, 15, 23)

$$a \ll \frac{0.09}{2\pi} \frac{1}{(1 - \mu_c)^{1/2}} \tau_p v_j \sin \beta \cos \beta, \quad (27)$$

and for the mass of the jet source, m_j , (Eqs. 11, 14, 15, 23)

$$m_j \ll \frac{0.09}{8\pi^3} \frac{(1 - \mu_c)^{1/2}}{\mu_c^2} \tau_p v_j^3 \sin^3 \beta \cos \beta. \quad (28)$$

5.6. Fitting procedure

For the fitting process we consider as known the inclination angle of the jet axis with respect to the plane of the sky, i . As discussed in López et al. (1996) and Anglada et al. (2007) the inclination angle is small, and so, the model depends weakly on i . We have taken $i = 5^\circ$. Another parameter considered as known is the offset in the y direction of the HH 30 star position with respect to the intensity peak of HH 30 (knot A0). We have taken $-0''.51$, the same value as in Anglada et al. (2007).

The model of variable velocity jet was used to fit the x positions of the knots A to E of the jet and the knots Z1 to Z6 of the counterjet in the 2010 image (Tables 2 and 3). The knot D4 of the jet was excluded from the fit because it was identified only in the 2010 image and its proper motion could not be measured.

The fitting strategy was to sample the six-dimensional parameter space, defined by the parameters $m\mu_c^3$, τ_o , β , φ_o and φ_p . Several sampling methods were tested, i.e. regular grid, random, and Halton sequence (Halton 1964). We discarded the regular grid method because some parameters (for instance, τ_o) can have evenly spaced values that fit the data. We adopted a Halton quasi-random sequence because it samples the space parameter more evenly than a purely random sequence, and the convergence of the fitting procedure to the minimum of the rms residual is faster.

Several runs of the fitting procedure were performed using different number of sample points (typically between 10^6 and 10^7), and different ranges of the parameters. The “pure” orbital model, depending three parameters, $m\mu_c^3$, τ_o , and φ_o was also fitted, by adopting a fixed value $\beta = 0$.

Once a minimum of the rms fit residual was found, the uncertainty in the parameters fitted was found as the increment of each of the six (or three) parameters of the fit necessary to increase the rms fit residual a factor of $(1 + \chi_p^2/n)^{1/2}$, where n is the number of knots whose position was fitted, p is the number of parameters fitted, and χ_p^2 is the value of χ^2 for p degrees of freedom (the number of free parameters) and 68% significance ($1-\sigma$ uncertainty), i.e. $\chi_3^2 = 3.53$, $\chi_6^2 = 7.04$ (Lampton et al. 1976).

5.7. Results of the model fitting

Let us first consider a system where precession and orbital motion are present in the jet, and both contribute to determine the shape of the jet. This condition means that the half-opening angles due to orbital motion, α , and to precession, β , are of the same order. For the range of masses considered for the HH 30 jet source and the companion (0.06 – $1 M_\odot$; see below), the orbital period is substantially shorter than the precession period.

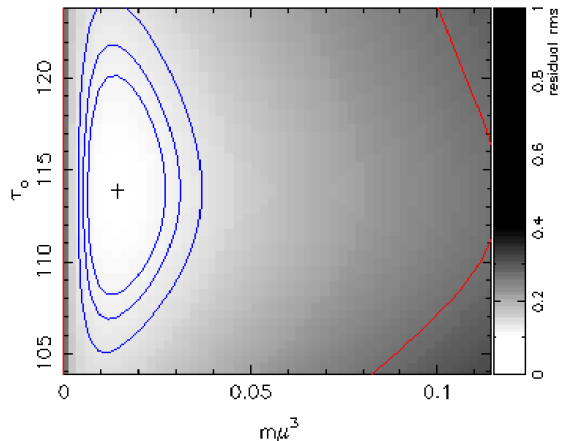


Figure 9. Rms fit residual of the “pure” orbital model fitted to the HH 30 knots of the jet and counterjet, as a function of mass function $m\mu_c^3$ and orbital period τ_o . The cross marks the position of the best fit, for which the rms is $0''.104$. The blue contours indicate the confidence levels 68% ($1-\sigma$ uncertainty), 90%, and 99%, while the red contour indicates the rms x position of the knots with respect to the jet axis, $0''.272$.

Thus, the jet shapes obtained from the model present a short-scale wiggling corresponding to the orbital period τ_o , and a large-scale wiggling corresponding to the precession period τ_p (see, for instance, Fig. 3 of Raga et al. 2009b). Although such a kind of model can reproduce the observed x positions of the limited number of knots included in the fitting, it predicts a small-scale wiggling shape between these knots, which is not observed in the HH 30 jet images. Thus, the model that fits the data has to be either precession-dominant ($\alpha \ll \beta$), or orbital-motion-dominant ($\beta \ll \alpha$).

The precession-dominant model can be excluded from simple considerations. Since the observed wiggles of the jet in the plane of the sky have a wavelength of $\sim 16''$ (Anglada et al. 2007, see also Fig. 14), a jet velocity of $v_j \simeq 100 \text{ km s}^{-1}$ would result in $\tau_p \simeq 100$ yr, assuming a precession-dominant scenario. Since the observed half-opening angle of the jet cone is $\sim 1.5^\circ$ (Anglada et al. 2007), and $\alpha \ll \beta$, the precession angle should be $\beta \simeq 1.5^\circ$. We know that the mass of the jet source cannot be higher than $\sim 1 M_\odot$. Higher values of the mass are unlikely since the bolometric luminosity of the system is less than $1 L_\odot$ (Cotera et al. 2001). It can neither be lower than the mass of a brown dwarf, $\sim 0.06 M_\odot$. Using these constraints and Eqs. 27, 28, we can derive an upper limit for the binary separation for the allowed range of masses of the jet source. The value obtained for the binary separation in all cases is $a \ll 1$ AU. This is extremely improbable since the radius of the accretion disk should be even smaller, while typical sizes of accretion disks are more than one order of magnitude larger. It is worth noting that Anglada et al. (2007) obtain higher values of the proper motion velocities ($\sim 200 \text{ km s}^{-1}$), resulting in a smaller value for the estimated period, $\tau_p \simeq 53$ yr, that did not allow them to discard a precession-dominant scenario for the allowed range of masses. Thus, the wiggles observed in the plane of the sky have to be mainly caused by the orbital motion of the jet source. Precession, if any, is not important for shaping the jet and counterjet.

In order to fit the shape of the jet and counterjet, we

Table 5
Results obtained from the fit to the jet and counterjet knots.^a

Parameter	(Units)	Value	Value	Value
Knots fitted		ABCE ^b	ABCDE ^b	ABCDEZ ^b
Initial rms	(arcsec)	0.360	0.321	0.272
Fit rms	(arcsec)	0.090	0.087	0.104
$m\mu_c^3$	(M_\odot)	0.016 ± 0.006	0.015 ± 0.009	0.014 ± 0.006
τ_o	(yr)	110.1 ± 1.8	110.6 ± 1.3	113.9 ± 1.7
φ_o^c	(rad)	2.23 ± 0.17	2.15 ± 0.17	1.65 ± 0.20
r_o	(AU)	5.8 ± 0.7	5.7 ± 1.1	5.7 ± 0.9
v_o	(km s^{-1})	1.6 ± 0.2	1.5 ± 0.3	1.5 ± 0.2
β^d	(deg)	0	0	0
m_j^e	(M_\odot)	0.06–1.0	0.06–1.0	0.06–1.0
μ_c^f		0.51–0.23	0.50–0.23	0.49–0.22
m_c^f	(M_\odot)	0.06–0.30	0.06–0.29	0.06–0.29
a^f	(AU)	11.4–25.1	11.4–25.1	11.5–25.6

^a Obtained for a distance $D = 140$ pc and assuming an inclination angle of the jet axis with respect to the plane of the sky $i = 5^\circ$.

^b Knot velocities used: $v_j = 98 \text{ km s}^{-1}$ (A, B, C, E, Z4); $v_j = 181 \text{ km s}^{-1}$ (Z1, Z3, Z5); $v_j = 234 \text{ km s}^{-1}$ (D); $v_j = 307 \text{ km s}^{-1}$ (Z2, Z6).

^c At the epoch $t_0 = 2010$ Dec 01.

^d Adopted (see text).

^e Range of masses considered for the jet source (see text).

^f The first value is for the minimum value of m_j , and the second one is for the maximum.

proceeded in various steps. For each step we used the procedure described in §5.6. First we fitted the “pure” orbital model to the knots of the jet that move at a similar (low) velocity, and where the wiggling is more evident: knots A, B, C, and E. For these knots we adopted the same velocity, the error-weighted average of their velocities, 98 km s^{-1} . The result of this first fit is shown in Table 5.

The next step was to include in the fit the rest of knots of the jet, the high-velocity knots D. For these knots, we also adopted as velocity the error-weighted average of their velocities, 234 km s^{-1} (see Fig. 3). The same values (within errors) of the parameters obtained for the first fit, were able to fit all the knots of the jet (see Table 5).

The third step was to include in the fit the knots of the counterjet. As stated before, the knots of the counterjet have very different velocities. We classified the counterjet knots into three groups. The medium-velocity group is formed by knots Z1, Z3, Z5a, and Z5b. Their error-weighted average velocity is 181 km s^{-1} . The low-velocity group contains only one knot, Z4, for which we adopted the same velocity as the low-velocity knots of the jet, 98 km s^{-1} . Finally, the extremely-high velocity group, with knots Z2 and Z6, for which we adopted the error-weighted average of their velocities, 307 km s^{-1} (see Fig. 3). Once again, the same values (within errors) of the parameters obtained for the first fit, were able to fit all the knots of the jet and counterjet (see Table 5).

The last step was to include precession in the model, as a perturbation of the orbital motion (i.e. for $\beta \ll \alpha$). However, for this last fit the parameters of the precession were not well constrained by the data, and the rms fit residual did not improve with the inclusion of precession.

Thus, we consider that the best fit to the shape of the jet and counterjet is an orbital model, with a mass function $m\mu_c^3 = 0.014 \pm 0.006 M_\odot$, an orbital period $\tau_o = 114 \pm 2$ yr, and an orbital phase angle $\varphi_o = 1.65 \pm 0.20$

Table 6
Favored set of parameters of the HH 30 binary system^a.

τ_o^b (yr)	v_o^c (km s^{-1})	φ_o^d (deg)	$m_j^{e,f}$ (M_\odot)	$m_c^{e,g}$ (M_\odot)	$a^{e,h}$ (AU)
114 ± 2	1.5 ± 0.2	95 ± 11	0.31 ± 0.04	0.14 ± 0.03	18.0 ± 0.6

^a Obtained for a distance $D = 140$ pc and assuming an inclination angle of the jet axis with respect to the plane of the sky $i = 5^\circ$.

^b Orbital period.

^c Orbital velocity.

^d Orbital phase angle with respect to an axis perpendicular to the line of sight, at the epoch 2010 Dec 01.

^e Assuming a mass of the system $m = 0.45 \pm 0.04 M_\odot$ (Pety et al. 2006).

^f Mass of the jet source.

^g Mass of the companion star.

^h Binary separation.

rad at $t_0 = 2010$ Dec 01. In Fig. 9 we show the rms fit residual as a function of the mass function $m\mu_c^3$ and orbital period τ_o , around the best-fit values. The shape of the jet obtained from this model is shown in Fig. 10, where the continuum line indicating the shape of the jet has been obtained by interpolating the velocities adopted for the knots with a boxcar function, as shown in Fig. 3.

From the fitted parameters we obtain a radius of the absolute orbit $r_o = 5.7 \pm 0.9$ AU, and an orbital velocity $v_o = 1.5 \pm 0.2 \text{ km s}^{-1}$. The orbital velocity obtained is low, similar to that obtained for other jets in young stellar objects. For instance, in HH 111, $v_o = 3.1 \pm 1.9 \text{ km s}^{-1}$ (Noriega-Crespo et al. 2011), and in HH 211, $v_o = 1.6 \pm 0.6 \text{ km s}^{-1}$ (Lee et al. 2010).

The values of the mass of the jet source and companion are not constrained by the fit. For the range of possible masses of the jet source $m_j = 0.06\text{--}1 M_\odot$ (see above), we obtain that the companion has a range of masses $m_c = 0.06\text{--}0.29 M_\odot$, and the binary separation (radius of the

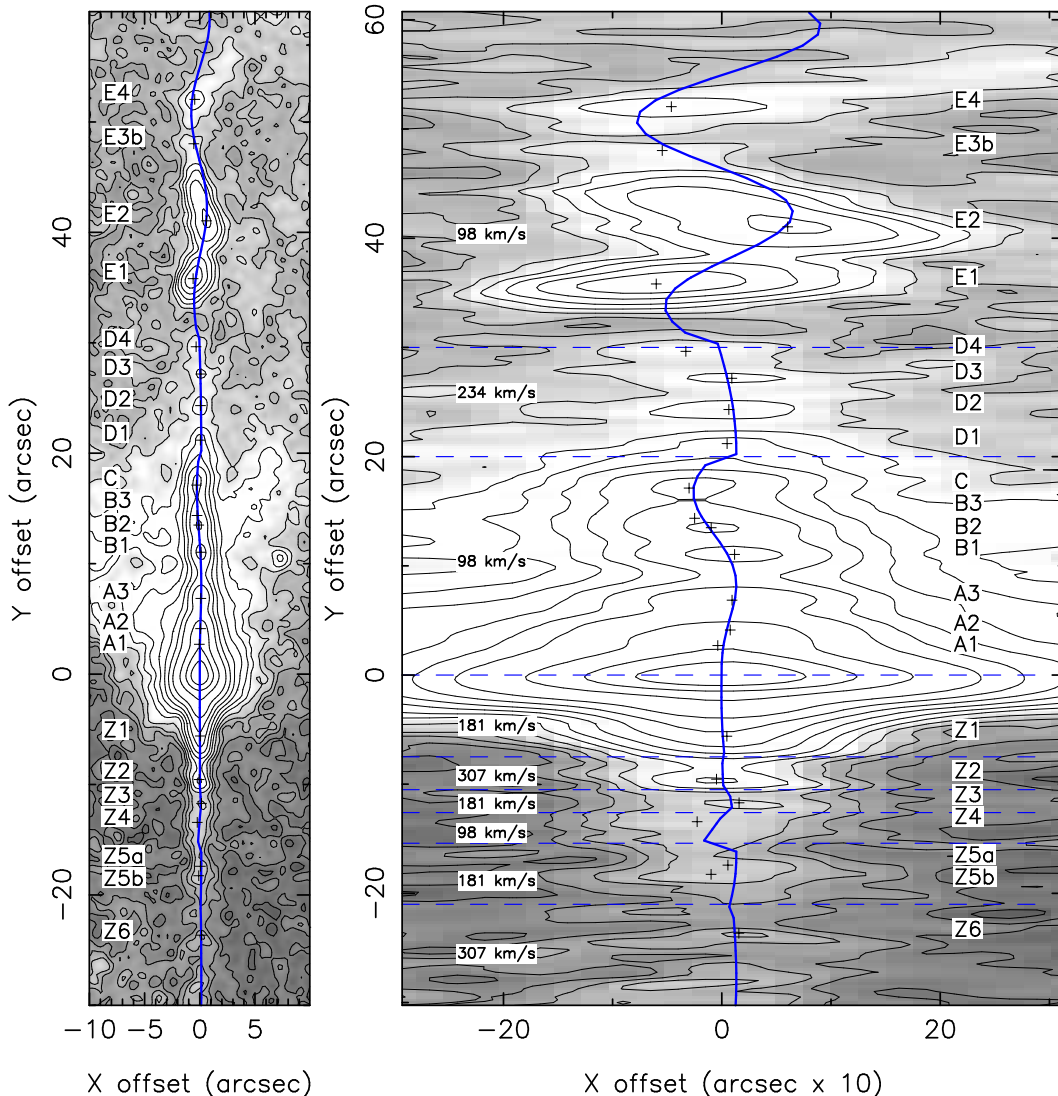


Figure 10. 2010 [SII] narrow-band image of the jet and counterjet of HH 30, between $-30''$ and $+60''$ of the HH 30 star. *Left:* Same scale in x and y . *Right:* x scale amplified a factor of 10. The measured positions of the knots are marked with crosses. The rms x position of these knots with respect to the jet axis is $0''.272$. The continuum blue line is the jet shape calculated from the “pure” orbital model with a mass function $m\mu_c^3 = 0.014 \pm 0.006 M_\odot$, an orbital period $\tau_o = 114 \pm 2$ yr, and an orbital phase angle $\varphi_o = 1.65 \pm 0.20$ rad at $t_0 = 2010$ Dec 01. The rms fit residual in x is $0''.119$. The horizontal dashed lines mark the boundaries of the regions with different knot velocities. The knot velocities are indicated for each region.

relative orbit) is in the range $a = 11.5\text{--}25.6$ AU.

Pety et al. (2006) find evidence of Keplerian rotation of the circumbinary disk in their CO observations with the PdBI, and derive a value of $m = 0.45 \pm 0.04 M_\odot$ for the central stellar mass. Using this value of m and the parameters of the fit, we obtain a mass $m_j = 0.31 \pm 0.04 M_\odot$ for the jet source, a mass $m_c = 0.14 \pm 0.03 M_\odot$ for the companion, and a binary separation $a = 18.0 \pm 0.6$ AU.

6. DISCUSSION

Anglada et al. (2007) carry out a detailed study of the morphology and proper motions of the HH 30 jet. They find that the proper motion velocities of the jet knots were of the order of 200 km s^{-1} . They also find that the jet path shows a wiggling with a periodicity in the plane of the sky of $16''$ that translates into a period of 53 yr using the derived proper motion velocity. It is shown that this period and the observed shape of the jet can be

explained either by the orbital motion of the jet source or by precession of the jet axis because of tidal interactions of a companion star. In the first case, the binary separation would be 9-18 AU, while in the precession scenario the binary separation would be < 1 AU. In either of the two scenarios the binary separation is much smaller than the radius (~ 250 AU) of the disk observed with the HST (Burrows et al. 1996; Stapelfeldt et al. 1999), showing that it is a circumbinary rather than a circumstellar disk, and that it cannot play a role in the jet collimation. The true circumstellar disk associated with the HH 30 jet should be found at scales of a fraction of the binary separation. In case of wiggling produced by orbital motion, the jet/counterjet system is expected to present plane (“C”) symmetry with respect to the equatorial plane, while in the case of precession the jet/counterjet system is expected to present point symmetry with respect to the position of the driving source. Since the images obtained by Anglada et al. (2007) only cover a small por-

tion of the counterjet, they cannot discriminate between the two alternative scenarios.

In this paper we presented new observations that allowed us to image and measure proper motions both in the jet and in the counterjet. In principle, these new data should be able to distinguish between the orbital and precession scenarios. For instance, in HH 111 (Noriega-Crespo et al. 2011) and HH 211 (Lee et al. 2010) plane symmetries in the jet/counterjet indicative of orbital motion of the driving source have been recently found. Unfortunately, the counterjet of HH 30 is weak, and appears less ordered than the jet, with larger variations in the velocity of the knots. So, it is not expected to show a clear symmetry as a constant velocity wiggling jet would do.

Interestingly, our new observations, covering a longer time span, allowed us to derive more accurate proper motions and reveal that the velocities of the knots are smaller than the values estimated by Anglada et al. (2007). The new values of the proper motions imply that the wiggling period is about twice the previous value (114 yr instead of 53 yr), allowing us to discard a significant contribution of precession to the observed wiggling of the jet (see §5.7).

Thus, based on our new observations we conclude that the observed shape of the jet is a consequence of the orbital motion of the jet source in a binary system. From our new results, and assuming that the central stellar mass is $m = 0.45 \pm 0.04 M_{\odot}$, as estimated by Pety et al. (2006) from the CO kinematics of the disk, we obtain that the binary separation (i.e. the radius of the relative orbit) should be 18.0 ± 0.6 AU. Interestingly, Guilloteau et al. (2008) observe a hole of 37 ± 4 AU of radius in the CO and dust emission from the disk associated with HH 30. These authors interpret this hole as produced by tidal effects in a binary system, inferring a binary separation of 18 ± 2 AU, in excellent agreement with our result. Therefore, these results give strong support to the binary interpretation, and in particular to the orbital motion scenario we proposed for HH 30.

A binary separation of 18 AU corresponds to an angular separation of $0''.13$ at a distance of 140 pc. Thus, the proposed binary system associated with the HH 30 jet can be angularly resolved by the new, expanded Jansky Very Large Array (JVLA) and by the Atacama Large Millimeter/submillimeter Array (ALMA). Unfortunately, according to our modeling of the orbital motion, at the current epoch (~ 2012.5) the two stars are roughly aligned along the line of sight ($\theta_o = 100^\circ$), resulting in a projected angular separation of $0''.02$, which is too small to be angularly resolved by the currently available instrumentation. We should wait four years until the projected angular separation will reach $\gtrsim 0''.05$ and the presence of the proposed binary system could be confirmed by a direct observation of a double source and/or to measure orbital proper motions, as has been done previously in other binary young stellar objects (e.g. L1551-IRS5; Rodríguez et al. 2003)

When the HST observations revealed the silhouette of a flared edge-on disk with a radius of ~ 250 AU perpendicular to the HH 30 jet, this system was considered the archetype of a jet/circumstellar accretion disk system in a young stellar object. However, the discovery that the central source is in fact a binary, and therefore, that

the disk is circumbinary rather than circumstellar, has changed our understanding of this object. Tidal truncation of the disk in a binary system suggests that the radius of the circumstellar disk should be about $\sim 1/3$ of the binary separation (e.g. Terquem et al. 1999). Thus, we expect that the “true” circumstellar accretion disk associated with the driving source of the HH 30 jet must have a radius $\lesssim 6$ AU. Therefore, the search for this circumstellar disk should be carried out at very small scales ($\sim 0''.05$)

Another interesting characteristic of the HH 30 system is that the jet and counterjet show clear differences. The knots of the jet and of the counterjet cannot be grouped in pairs with similar separation from the star and similar velocity. HH 30 seems to be, in this aspect, completely different, for instance, from the jet and counterjet of HH 34, in which the jet and counterjet show a remarkable symmetry (Raga et al. 2011). Clear jet/counterjet asymmetries in the physical properties have been found in several well studied jets, such as DG Tau B (Podio et al. 2011), FS Tau B (Liu et al. 2012), DG Tau (Agra-Amboage et al. 2011), or HH 30 itself (Bacciotti et al. 1999). Actually, strong velocity asymmetries between the red and blue lobes are frequent. Hirth et al. (1994) note that about half of bipolar jets present a strong asymmetry of about a factor two in velocity between the two lobes. In HH 30 we found that the average proper motion velocities in the counterjet are a factor of 1.7 higher than in the jet. We also found a higher velocity dispersion in the counterjet (see §3). In the frame of stellar wind models, velocity asymmetries between the jet and counterjet have been attributed to differences in pressure. In the frame of magneto-hydrodynamical disk winds, jet asymmetries require an asymmetry in magnetic lever arms or in launch radii between either sides of the disk, a situation that may occur naturally in an asymmetric ambient medium. For example, if the ambient radiation field is stronger on one side, this can increase the level of ionization on the surface of the disk on that side, leading to enhanced mass load on the magnetic field lines (smaller magnetic lever arm), and/or to a larger jet launching region (see Ferreira et al. 2006).

However, HH 30 also shows differences in velocity in the same lobe of the outflow. For the jet, there are at least two velocities, a low velocity of ~ 100 km s $^{-1}$ for knots A, B, C, and E, and a high velocity of ~ 240 km s $^{-1}$ for knots D. For the counterjet we find knots close to each other with different velocities, and there are at least three different velocities, a low velocity of ~ 100 km s $^{-1}$ for knot Z4, a medium velocity of ~ 180 km s $^{-1}$ for knots Z1, Z3, Z5a and Z5b, and an extremely-high velocity of > 300 km s $^{-1}$ for knots Z2 and Z6 (see §3). Indeed, we found that the knots Z1 and Z2 (and perhaps also Z5 and Z6) of the counterjet appear to be launched nearly simultaneously with very different velocities. These strong differences in velocity for knots located in the same lobe of the outflow cannot be attributed only to asymmetries in the ambient medium between the two sides of the disk. Therefore, launching from different radii in an extended disk wind scenario provides the simplest explanation for the different observed velocities. Following Blandford & Payne (1982), the asymptotic jet velocity as a function of the

launch radius in the disk, r_l , is expected to be of the order of $\sim 100(M_*/0.5 M_\odot)^{1/2}(r_l/1 \text{ AU})^{-1/2} \text{ km s}^{-1}$ for a value of the magnetic lever arm parameter of ~ 10 (i.e. “the extended warm disk wind scenario with moderate lever arms” described, e.g. in Ferreira et al. 2006; Panoglou et al. 2012, and references therein). Assuming that the jet source has a mass of $0.31 M_\odot$ (see above), we obtain that a range of launching radii $r_l = 0.07\text{--}0.6 \text{ AU}$ is required to explain the velocity range of $\sim 100\text{--}300 \text{ km s}^{-1}$ observed in the HH 30 jet/counterjet. This range of launching radii falls within the range of values determined for T Tauri jets (e.g. Anderson et al. 2003; Pesenti et al. 2004; Ferreira et al. 2006, and references therein), which range from 0.07 AU (the typical disk corotation radius) up to $\sim 3 \text{ AU}$.

7. CONCLUSIONS

Using data from observations at six different epochs, we have measured the proper motions and studied the morphology of the HH 30 jet/counterjet system. Our main conclusions are summarized in the following.

- The motion of most knots is essentially ballistic, but the jet/counterjet shows a large scale bending. This bending can be produced by a relative motion of the HH 30 star with respect to its surrounding environment of $\sim 2 \text{ km s}^{-1}$, caused either by a possible proper motion of the HH 30 star, or by the entraining of environment gas by the red lobe of the nearby L1551-IRS 5 outflow. Alternatively, the bending can be produced by the stellar wind from a nearby CTTS, identified in the 2MASS catalog as J04314418+181047.
- The average velocity of the knots of the jet is about twice than that of the counterjet. Velocity differences are also found in the same outflow lobe. Most of the knots of the jet move at velocities of $\sim 100 \text{ km s}^{-1}$, but several knots (knots D) move faster, at $\sim 240 \text{ km s}^{-1}$. The velocities of the counterjet knots are less ordered, with knots moving, at least, at three different velocities of about 100, 180, and $\gtrsim 300 \text{ km s}^{-1}$. In particular, we identified at least a pair of knots in the counterjet (knots Z1 and Z2) that apparently have been launched simultaneously with very different velocities.
- The asymmetry in the average velocities of the jet and counterjet may be due to an asymmetric ambient medium. The observed differences in velocity of the knots of the same outflow lobe can be attributed to different launching radii in an extended “warm” disk wind scenario. The range of launching radii in the circumstellar accretion disk required to account for the observed range of velocities of the knots is $\sim 0.07 \text{ AU}$ to $\sim 0.6 \text{ AU}$, which falls within the range of typical values determined for T Tauri jets.
- The observed wiggling of the HH 30 jet and counterjet is produced by the orbital motion of the jet source in a binary system. Precession of the accretion disk, if present at all, appears to be a minor contribution in shaping the jet. The best fit to the

shape of the jet is obtained with a binary system with a mass function $m\mu_c^3 = 0.014 \pm 0.006 M_\odot$, an orbital period $\tau_o = 114 \pm 2 \text{ yr}$, and an orbital velocity of $v_o = 1.5 \pm 0.2 \text{ km s}^{-1}$. Adopting a value of the total stellar mass of $m = 0.45 \pm 0.04 M_\odot$ (Pety et al. 2006), we obtain that the mass of the jet driving source is $m = 0.31 \pm 0.04 M_\odot$, the mass of the companion is $m = 0.14 \pm 0.03 M_\odot$, and the binary separation is $18 \pm 0.6 \text{ AU}$. The same value of the binary separation is inferred from the size of the inner cavity observed in the circumbinary disk (Guilloteau et al. 2008), assuming it is produced by tidal truncation of the disk in a binary system. This result strongly supports our binary interpretation first proposed by Anglada et al. (2007).

In summary, the HH 30 jet/counterjet system appears to originate likely from a binary system of two stars of masses $0.31 M_\odot$ (the jet driving source) and $0.14 M_\odot$, separated 18 AU and orbiting with a period of 114 yr. The system is surrounded by a circumbinary disk with an outer radius of $\sim 250 \text{ AU}$ and with an inner radius $\sim 40 \text{ AU}$. The driving source of the jet/counterjet appears to be surrounded by a circumstellar accretion disk with an outer radius $\lesssim 6 \text{ AU}$, and probably with an inner radius of $\sim 0.07 \text{ AU}$. The observed jet/counterjet knots reach velocities in the range $\sim 100\text{--}300 \text{ km s}^{-1}$, arising from disk radii ranging from 0.07 AU to 0.6 AU. The two components of the binary system are currently roughly aligned along the line of sight, but their angular separation in the plane of the sky and orbital motions could be determined by future observations with the JVL A or ALMA

G. A., R. E., R. L., A. R., and C. C.-G. are partially supported by Spanish MCI grants AYA2008-06189-C03 and AYA2011-30228-C03, and FEDER funds. We acknowledge Pau Estalella for his helpful comments on the use of the Halton sequence. The data presented here were taken at the 2.5 m Isaac Newton Telescope, the 4.2 m William Herschel Telescope, and the 2.6 m Nordic Optical Telescope at the Observatorio del Roque de los Muchachos of the Instituto de Astrofísica de Canarias.

REFERENCES

- Agra-Amboage, V., Dougados, C., Cabrit, S., & Reunanen, J. 2011, *A&A*, 532, A59
- Anderson, J. M., Li, Z.-Y., Krasnopolsky, R., Blandford, R. D. 2003, *ApJ*, 590, L107
- Anglada, G., López, R., Estalella, R., Masegosa, J., Riera, A., & Raga, A.C. 2007, *AJ*, 133, 2799.
- Bacciotti, F., Eisloffel, J., & Ray, T. P. 1999, *A&A*, 350, 917
- Blandford, R. D., & Payne, D. G. 1982, *MNRAS*, 199, 883
- Burrows, C. J., Stapelfeldt, K. R., Watson, A. M., Krist, J. E., Ballester, G. E., Clarke, J. T., Crisp, D., Gallagher, J. S., Criffiths, R. E., Hester, J. J., Hoessel, J. G., Holtzman, J. A., Mould, J. R., Scowen, P. A., Trauger, J. T., & Westphal, J. A., 1996, *ApJ*, 473, 437
- Cantó, J., & Raga, A. C. 1995, *MNRAS*, 277, 1120
- Cotera, A. S., Whitney, B. A., Young, E., Wolff, M. J., Wood, K., Povich, M., Schneider, G., Rieke, M., & Thompson, R. 2001, *ApJ*, 556, 958
- De Colle, F., del Burgo, C., & Raga, A.C. 2010 *ApJ*, 721, 929
- Durán-Rojas, M. C., Watson, A. M., Stapelfeldt, K. R., & Hiriart, D. 2009, *AJ*, 137, 4330
- Esquivel, A., Raga, A. C., & De Colle, F. 2007, *A&A*, 468, 613

- Ferreira, J., Dougados, C., & Cabrit, S. 2006, *A&A*, 453, 785
- Graham, J. A., & Heyer, M. H. 1990, *PASP*, 102, 972
- Guilloteau, S., Dutrey, A., Pety, J., & Gueth, F. 2008, *A&A*, 478, L31
- Halton, J. H. 1964, *Commun. ACM*, 7, 701
- Hartigan, P., & Morse, J. 2007, *ApJ*, 660, 426
- Hartmann, L. 2005, *ASP Conf. Ser.* 337, 3
- Hirth, G. A., Mundt, R., Solf, J., & Ray, T. P. 1994, *ApJ*, 427, L99
- Kenyon, S. J., Brown, D. I., Tout, C. A., & Berlind, P. 1998, *AJ*, 115, 2491
- Kenyon, S.J., Dobrzycka, D., & Hartmann, L. 1994, *AJ*, 108, 1872
- Lada, C. J., & Adams, F. C. 1992, *ApJ*, 393, 278
- Lampton, M., Margon, B., & Bowyer, S. 1976 *ApJ*, 208, 177
- Lee, C.-F., Hasegawa, T. I., Hirano, N., Palau, A., Shang, H., Ho, P. T. P., Zhang, Q. 2010 *ApJ*, 713, 731
- Liu, C.-F., Shang, H., Pyo, T.-S., Takami, M., Walter, F. M., Yan, C.H., Wang, S.-Y., Ohashi, N., Hayashi, M. 2012 *ApJ*, 749, 62
- López, R., Raga, A. C., Riera, A., Anglada, G., & Estalella, R., 1995, *MNRAS*, 274, L19
- López, R., Riera, A., Raga, A. C., Anglada, G., López, J. A., Noriega-Crespo, A., & Estalella, R., 1996, *MNRAS*, 282, 470
- Madlener, D., Wolf, S., Dutrey, A., & Guilloteau, S., 2012, *A&A*, in press (arXiv:1205.4901v1 [astro-ph.SR])
- Masciadri, E., & Raga, A. C. 2002, *ApJ*, 568, 733
- Montgomery, M. M. 2009, *MNRAS*, 394, 1897
- Mundt, R., Brugel, E. W., & Bührke, T., 1987, *ApJ*, 319, 275
- Mundt, R. & Fried, J. W., 1983, *ApJ*, 274, 83
- Mundt, R., Ray, T. P., & Bührke, T., 1988, *ApJ*, 333, L69
- Mundt, R., Ray, T. P., Bührke, T., Raga, A. C., & Solf, J., 1990, *A&A*, 232, 37
- Mundt, R., Ray, T. P., & Raga, A. C., 1991, *A&A*, 252, 740
- Noriega-Crespo, A., Raga, A. C., Lora, V., Stapelfeldt, K. R., Carey, S. J. 2011, *ApJ*, 732, L16
- Panoglou, D., Cabrit, S., Pineau Des Forêts, G., Garcia, P. J. V., Ferreira, J., & Casse, F. 2012, *A&A*, 538, A2
- Pesenti, N., Dougados, C., Cabrit, S., Ferreira, J., Casse, F., Garcia, P., O'Brien, D. 2004, *A&A*, 416, L9
- Pety, J., Gueth, F., Guilloteau, S., & Dutrey, A. 2006, *A&A*, 458, 841
- Podio, L., Eislöffel, J., Melnikov, S., Hodapp, K. W., & Bacciotti, F. 2011, *A&A*, 527, A13
- Raga, A. C., Cantó, J., Rodríguez-González, A., & Esquivel, A. 2009a, *A&A*, 493, 115
- Raga, A. C., Esquivel, A., Velázquez, P. F., Cantó, J., Haro-Corzo, S., Riera, A., & Rodríguez-González, A. 2009b *ApJ*, 707, L6
- Raga, A. C., López, R., Riera, A., Estalella, R., & Anglada, G. 1997, *Rev. Mex. Astron. Astrof.*, 33, 127
- Raga, A. C., Noriega-Crespo, A., Lora, V., Stapelfeldt, K. R., Carey, S. J. 2011, *ApJ*, 730, L17
- Ray, T. P., Mundt, R., Dyson, J. E., Falle, S. A. E. G., & Raga, A. C. 1996, *ApJ*, 468, L103
- Rodríguez, L. F., Curiel, S., Cantó, J., Loinard, L., Raga, A. C., Torrelles, J. M. 2003, *ApJ*, 583, 330).
- Roman-Lopes, A. 2009, *MNRAS*, 398, 1368
- Stapelfeldt, K. R., Watson, A. M., Krist, J. E., Burrows, C. J., Crisp, D., Ballester, G. E., Clarke, J. T., Evans, R. W., Gallagher, J. S. III, Griffiths, R. E., Hester, J. J., Hoessel, J. G., Holtzman, J. A., Mould, J. R., Scowen, P. A., & Trauger, J. T. 1999, *ApJ*, 516, L95
- Terquem, C. E. J. M. L. J. 1998, *ApJ*, 509, 819
- Terquem, C., Eislöffel, J., Papaloizou, J. C. B., & Nelson, R. P. 1999, *ApJ*, 512, L131
- Vrba, F. J., Rydgren, A. E., & Zak, D. S. 1985, *AJ*, 90, 2074
- Watson, A. M. & Stapelfeldt, K. R. 2007, *AJ*, 133, 845